A&A 386, 658–673 (2002)
DOI: 10.1051/0004-6361:20020252

Astronomy & Astrophysics

Spatially resolved microwave oscillations above a sunspot⋆

A. Nindos[1], C. E. Alissandrakis[1], G. B. Gelfreikh[2], V. M. Bogod[3], and C. Gontikakis[4]

[1] Section of Astrogeophysics, Physics Department, University of Ioannina, Ioannina 45110, Greece
[2] Main (Pulkovo) Astronomical Observatory, Russian Academy of Sciences, St.–Petersburg 196140, Russia
[3] St.–Petersburg Branch of the Special Astrophysical Observatory, Russian Academy of Sciences, Pulkovo, St.–Petersburg 196140, Russia
[4] Research Center for Astronomy and Applied Mathematics, Academy of Athens, 14 Anagnostopoulou Str., Athens 10673, Greece

Received 17 December 2001 / Accepted 28 January 2002

Abstract. Using high quality VLA observations, we detected for the first time spatially resolved oscillations in the microwave total intensity (I) and circular polarization (V) emission of a sunspot–associated gyroresonance (g–r) source. Oscillations were detected at 8.5 and 5 GHz during several time intervals of our 10–hour–long dataset. The oscillations are intermittent: they start suddenly and are damped somehow more gradually. Despite their transient nature when they are observed they show significant positional, amplitude and phase stability. The spatial distribution of intensity variations is patchy and the location of the patches of strong oscillatory power is not the same at both frequencies. The strongest oscillations are associated with a small region where the 8.5 GHz emission comes from the second harmonic of the gyrofrequency while distinct peaks of weaker oscillatory power appear close to the outer boundaries of the 8.5 and 5 GHz g–r sources, where the emissions come from the third harmonic of the gyrofrequency. Overall, the 5 GHz oscillations are weaker than the 8.5 GHz oscillations (the rms amplitudes of the I oscillations are 1.3–2.5 $\times 10^4$ K and 0.2–1.5 $\times 10^5$ K, respectively). At both frequencies the oscillations have periods in the three–minute range: the power spectra show two prominent peaks at 6.25–6.45 mHz and 4.49–5.47 mHz. Our models show that the microwave oscillations are caused by variations of the location of the third and/or second harmonic surfaces with respect to the base of the chromosphere–corona transition region (TR), i.e. either the magnetic field strength or/and the height of the base of the TR oscillates. The best–fit model to the observed microwave oscillations can be derived from photospheric magnetic field strength oscillations with an rms amplitude of 40 G or oscillations of the height of the base of the TR with an rms amplitude of 25 km. Furthermore, small variations of the orientation of the magnetic field vector yield radio oscillations consistent with the observed oscillations.

Key words. Sun: corona – Sun: radio radiation – Sun: oscillations – Sun: sunspots – Sun: magnetic fields

1. Introduction

The atmosphere above sunspots shows modes of oscillatory behavior. The oscillations are visible as intensity and velocity variations (see the review by Lites 1992). In the umbral photosphere, oscillations with periods in the five–minute range as well as in the three–minute range occur. At chromospheric levels the intensity and velocity oscillations with periods of 150–200 s show larger amplitudes and are observed in the inner part of the umbra. For a discussion of recent models of photospheric and chromospheric oscillations we refer the reader to the review by Staude (1999).

Recent studies have shown that photospheric magnetic field oscillations also exist (Rüedi et al. 1998; Norton et al. 1999; Balthasar 1999; Bellot Rubio et al. 2000) but they are limited to much smaller regions than the usual velocity oscillations. The origin of these oscillations is still under debate. Rüedi et al.'s (1998) observations of MDI oscillations suggest an origin in terms of magnetoacoustic gravity waves. On the other hand Bellot Rubio et al. (2000) suggest that their inferred magnetic field oscillations are caused by opacity fluctuations that move upward and downward the region where the spectral lines are sensitive to magnetic fields.

Observations with instruments on SOHO (Solar and Heliospheric Observatory) have revived interest in the TR oscillations (see Fludra 1999; Brylindsen et al. 1999a, 1999b; Maltby et al. 1999). The SOHO observations show that the 3–min oscillations usually affect the entire umbral

Send offprint requests to: A. Nindos,
e-mail: anindos@cc.uoi.gr

⋆ Tables 1–3 are only available in electronic form at http://www.edpsciences.org

TR and part of the penumbral TR. Most observations are compatible with the hypothesis that the oscillations are caused by linear, upward–propagating progressive acoustic waves (however, Brylindsen et al. 1999b reported nonlinear oscillations in the TR of one sunspot).

Independent information on oscillations in the TR/low corona has been provided by microwave observations of several strong stable gyroresonance (g–r) sunspot–associated sources (see White & Kundu 1997 for a review of the properties of the g–r mechanism). Using Nobeyama Radioheliograph (NoRH) data at 17 GHz, Gelfreikh et al. (1999) measured the circular polarization (V) flux of several such sources as a function of time and found nearly harmonic oscillations with periods mostly between 120–220 s. The periodic fluctuations of the V flux were interpreted in terms of MHD oscillations which result in variations of the size of the emitting gyroresonance layer and its temperature. Shibasaki (2001) detected 3–min oscillations in the 17 GHz emission of a sunspot for which 3–min velocity and intensity oscillations due to upward–travelling acoustic waves had been detected in TR lines observed by SUMER. Shibasaki (2001) applied the values of density and temperature fluctuations deduced from SUMER to the sunspot's gyroresonance emision and found good agreement with the detected radio oscillation. He attributed the 3–min oscillation to the resonant excitation of the cut–off frequency mode of the temperature plateau around the temperature minimum.

The fine structure of sunspot–associated sources is usually below the spatial resolution of the NoRH which is about $15''$. Therefore, Gelfreikh et al. (1999) and Shibasaki (2001) calculated the flux time profiles by integrating the emission over the entire 17 GHz source. Consequently they were not able to study the spatial distribution of oscillatory power above the sunspots. In this paper we search for oscillations in microwave sunspot g–r sources using multifrequency VLA[1] observations. Detection of periodic oscillations using VLA observations will advance our knowledge of this newly discovered phenomenon. The VLA can produce maps with smaller beams (about $1.5''$ at 15 GHz and $3''$ at 8 GHz). Thus using VLA maps, we can investigate the time fluctuations of individual components of a sunspot source rather than just the time variability of the source as a whole. Furthermore if the oscillations appear in more than one frequency, the VLA observations will allow us to study the appearance of the oscillation patterns at different heights in the corona.

2. Observations and data analysis

The VLA is a multi–configuration Fourier synthesis radio telescope (Napier et al. 1983) and was used in C configuration which provides high spatial resolution at the expense of reduced sensitivity to large sources due to the lack of sufficiently short baselines. Our observations were carried out on 2000 April 7. Our target was the sunspot of active region NOAA 8949 at 4.86 GHz (5 GHz), 8.47 GHz (8.5 GHz) and 14.98 GHz (15 GHz). The observations lasted 9 hours and 48 min (from April 7, 14:17 UT to April 8 00:05 UT). The heliographic coordinates of the center of the field of view at the middle of our observations was S18E53 at 15 and 8.5 GHz and S18E48 at 5 GHz. The time resolution of the observations is 10 s. The field of view at each wavelength is roughly $\theta_{\rm FOV} \approx 1.5\lambda_{\rm cm}$ arcmin (i.e. $3'$ at 15 GHz, $5.3'$ at 8.5 GHz and $9'$ at 5 GHz). At 5 GHz, active region NOAA 8948 was present at the west edge of the field of view. That active region underwent rapid changes associated with the emergence of new magnetic flux and will be presented elsewhere. During the first half of the observing time we sampled 15–min scans at 8.5 GHz interrupted by 10–min scans at the other frequencies. During the second half of the observations, we obtained successive 15–min scans at each frequency. For each frequency, originally we made maps using all available data. Then in order to detect oscillations we made snapshot maps. For all maps the standard CLEAN algorithm was used. At 8.5 and 5 GHz we used self–calibration to improve the dynamic range of the maps. At 15 GHz the self–calibration did not work because no strong sources were present in the field of view. The final maximum dynamic range of the snapshot maps are 12, 70 and 100 for the 15, 8.5 and 5 GHz total intensity (I) maps, respectively. The CLEAN beams of the final snapshot maps are about $5.7'' \times 5.3''$ at 5 GHz, $3.0'' \times 2.8''$ at 8.5 GHz and $1.4'' \times 1.1''$ at 15 GHz.

From about 22:46 UT untill the end of the VLA observations simultaneous NoRH observations were available. The NoRH consists of 84 antennas in a T–shaped array (Nakajima et al. 1994). It observes the full solar disk in two circular polarizations at 17 GHz. The NoRH data that overlapped with our VLA observations were processed in the NRAO software package AIPS and snapshot maps with a time resolution of 10 s were made, using techniques described by Nindos et al. (1999), Nindos et al. (2000) and Kundu et al. (2001). The size of the final restoring beam was about $17''$.

We also used MDI ("Michelson Doppler Imager" on board SOHO satellite) white light and magnetogram images. For the coregistration of optical and radio data we rotated the MDI images to the time of the radio images and then we used the known pointing information of the instruments. Unfortunately neither Hα nor SUMER/CDS images were available.

3. Overall view of the active region

The full–day radio images of the sunspot at 15, 8.5 and 5 GHz are presented in Fig. 1 as contour plots. The total intensity (I) maps are overlaid on an MDI white–light image and the circular polarization (V) maps are overlaid on an MDI magnetogram. At 15 GHz the emission is

[1] The Very Large Array is a facility of the National Radio Astronomy Observatory, which is operated by Associated Universities, Inc, under cooperative agreement with the National Science Foundation.

restricted to a small region over the umbra and is much weaker than at the lower frequencies. Since the peak I brightness temperature at 15 GHz is only about 25 000 K, it is clear that none of the gyroresonant surfaces contribute to the radio emission; hence the dominant emission mechanism should be free–free. The radio source at 15 GHz shows relatively low degree of circular polarization ρ_c (maximum about 15%) which is again consistent with free–free emission. The I emission at the lower frequencies is simple and peaks above the umbra, reaching million degree Kelvin values (1.3 MK and 2 MK at 8.5 and 5 GHz, respectively) and suggesting that gyroresonance is the dominant emission mechanism.

The typical ρ_c is about 30–50% and 10–30% at 8.5 and 5 GHz, respectively. The polarity of the sunspot's photospheric magnetic field is negative which corresponds to left circular polarizarion (LCP) for extraordinary mode (x–mode) emission. However, the V maps show right circular polarization (RCP) indicating that the radio emission crossed a region where the magnetic field is almost perpendicular to the line of sight and the sign of circular polarization was reversed. Furthermore the eastern (limbward) part of the I radio source is unpolarized. This can happen when both the third and second harmonics of the gyrofrequency are optically thick. However the 8.5 and 5 GHz I maps do not support such an interpretation because the corresponding I emissions are relatively low. Using a $500'' \times 500''$ area of the full–disk MDI magnetogram which contained the sunspot under study, we computed current–free extrapolations of the magnetic field (Alissandrakis 1981) at several heights above the photosphere. At heights above about 2×10^4 km the extrapolated negative polarity associated with the sunspot shrinks. Even higher up, the magnetic field is bipolar with the negative polarity coming from the excess flux of the sunspot's active region and the positive polarity coming from the active region which was located west of the sunspot's active region. As the height increases, the large–scale neutral line shifts towards the limb and coincides with the $V = 0$ area (the *depolarization line*) of the 8.5 GHz V map at a height of 1.05×10^5 km above the photosphere. Similar results for the behavior of the magnetic field with height were obtained by force–free extrapolations of the photospheric field with values of $|\alpha| < 4.1 \times 10^{-6}$ km^{-1}. Thus our calculations showed that the absence of polarized emission above the eastern part of the sunspot is a direct consequence of propagation effects. The situation is very similar to the one described in detail by Alissandrakis et al. (1996).

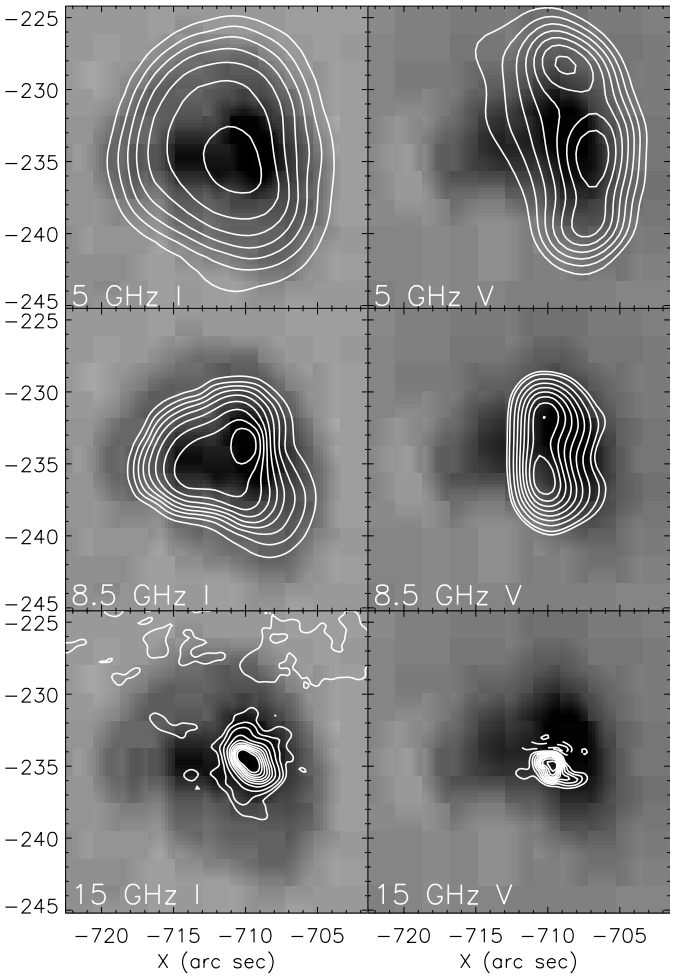

Fig. 1. Contour plots of the VLA maps. The I maps (left column) are overlaid on an MDI white light image observed at 22:23:33 UT and the V maps (right column) are overlaid on an MDI magnetogram obtained at 22:23:03 UT. The lowest contour and the contour step in the 15 GHz I map is 2500 K while the lowest contour in the 15 GHz V map is −800 K and the contour step is 400 K (dashed contours show negative brightness temperature). At 8.5 GHz the contours levels in the I map are (0.5, 0.75, 1, 2, 3, 5, 7.5, 10, 13)$\times 10^5$ K and the contour levels in the V map are (0.1, 0.25, 0.5, 0.75, 1, 2, 3, 4, 5)$\times 10^5$ K. At 5 GHz the contour levels in the I map are (0.5, 0.75, 1, 5, 10, 15, 20)$\times 10^5$ K and the contour levels in the V map are (0.1, 0.25, 0.75, 1, 2, 3, 4)$\times 10^5$ K. The axes denote distance from Sun's center. In this and subsequent images solar North is up and solar West to the right.

4. Oscillations of the microwave emission

We searched for oscillations of the sunspot–associated microwave emission by computing snapshot I and V maps at each frequency every 10 s for the entire period of the VLA observations. In order to enhance small intensity variations, we subtracted from each snapshot image the average image obtained using all data of each solar scan. Then for each difference image we calculated the standard deviation σ and we identified the radio sources with intensity more than 3σ. We calculated the time profiles and the corresponding power spectra of these radio sources.

At 15 GHz there was no difference image that contained pixels with intensities higher than its 3σ level and the power spectra analysis showed no oscillations. This negative result means either that radio oscillations did not exist at this frequency or that if they existed their amplitude would be lower than the typical rms amplitude of the 15 GHz emission variations which was 1500 K in I and 1100 K in V. The absence of oscillations was confirmed

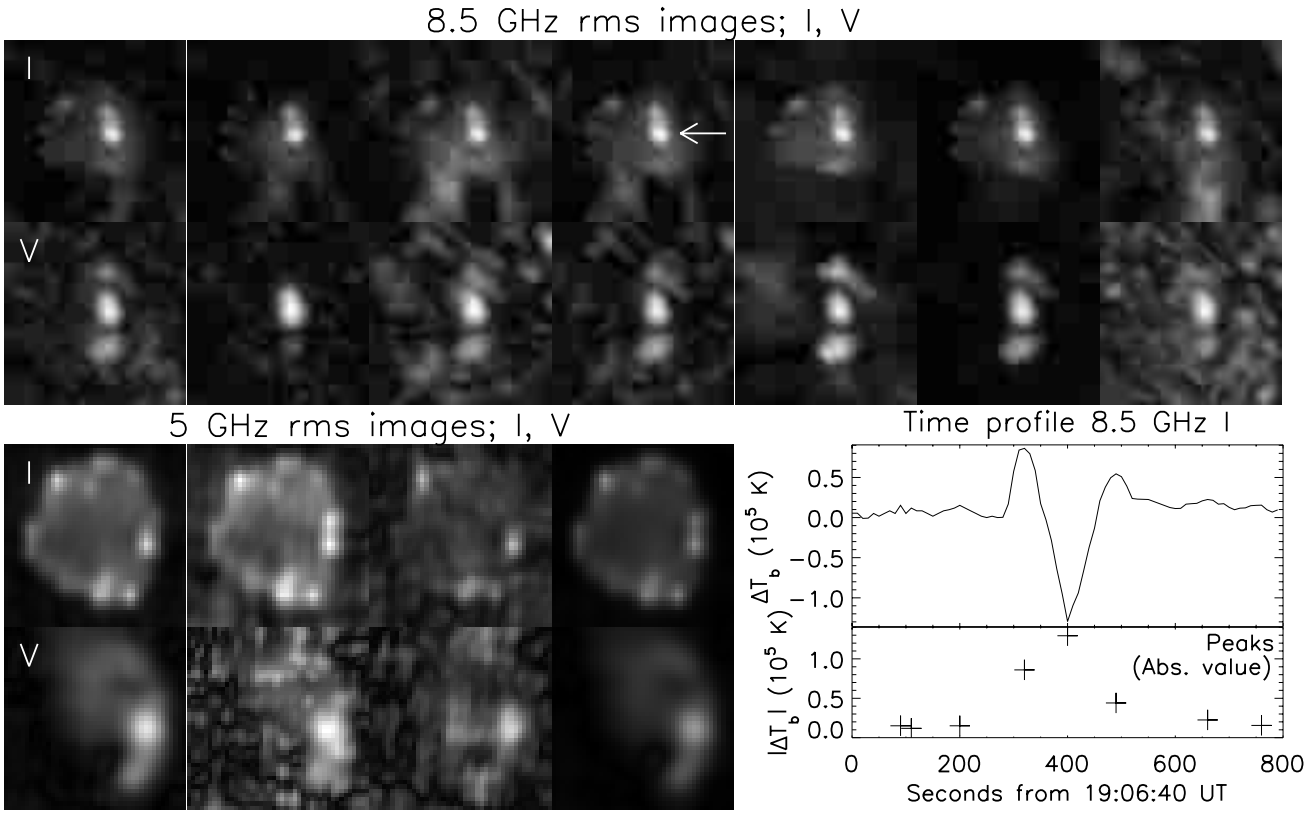

Fig. 2. Top row (from left to right): rms images for the sequences of 8.5 GHz I images obtained at 15:55:00–15:59:10 UT, 17:33:40–17:36:40 UT, 18:08:20–18:13:20 UT, 19:11:00–19:15:10 UT, 20:40:20–20:43:10 UT, 22:19:00–22:32:20 UT and 23:49:40–23:55:20 UT. Second row: same as top row for the corresponding 8.5 GHz V images. Third row images: rms images for the sequences of 5 GHz I images obtained at 15:08:10–15:11:10 UT, 18:48:40–18:53:20 UT, 20:06:00–20:09:20 UT and 21:40:00–21:53:20 UT. Bottom row images: same as third row for the corresponding 5 GHz V images. At the bottom half of the right part of the figure we show the time profile of the 8.5 GHz I source labeled with the arrow for the whole time interval of the corresponding solar scan. The time profile has been computed after the subtraction of the source's average intensity (over the whole scan) from the source's snapshot intensities. We also show the absolute value of the emission peaks.

by applying the above methodology to the 17 GHz NoRH snapshot maps obtained simultaneously with our VLA observations. We note that our 15 GHz source is weak and its emission comes from the free–free mechanism. Therefore it is quite different from the strong gyroresonance sources where Gelfreikh et al. (1999) and Shibasaki (2001) detected oscillations of the microwave emission.

Oscillations were detected at 8.5 and 5 GHz: the longest uninterrupted time intervals where oscillations were detected was between 22:19:00–22:32:20 UT at 8.5 GHz and between 21:40:00–21:53:20 UT at 5 GHz. Intensity variations with features similar to the intensity variations observed during these time intervals occurred during several shorter time intervals throughout the observations (see Table 1; the other entries of Table 1 will be discussed later). A first estimate of the I and V fluctuations for these sequences of images can be obtained from their rms values (e.g. see Tsiropoula et al. 2000) that we show in Fig. 2. It is interesting that at both frequencies the I and V fluctuations are not distributed uniformly above the sunspot source even though in most rms images the boundaries of the region that fluctuates roughly delineate the shape of the corresponding average image. Furthermore, at each frequency the same strong fluctuating sources can be identified in all rms images. In the following parts of the paper we shall focus our study on the 22:19:00–22:32:20 UT and 21:40:00–21:53:20 UT time series because they offer more opportunities for an in–depth analysis. We shall return to the other shorter duration oscillations toward the end of Sect. 4.

In Figs. 3 and 4 we present selected 8.5 GHz I and V difference images produced after the subtraction of the 22:19:00–22:32:20 UT average image from each snapshot image made during that time interval. Using the same methodology we computed 5 GHz snapshot difference images for 21:40:00–21:53:20 UT; selected images from this interval are presented in Figs. 5–6. The rightmost columns of Figs. 3–6 show the average and rms values of I and V emission.

At both frequencies, the difference images show no salt–and–pepper morphologies: this indicates a relatively high degree of coherence between the fluctuating elements. The snapshot difference images show that the intensity of the whole sunspot source changes as a function of time. However, some parts of the sunspot source fluctuate stronger than others and these fluctuations are

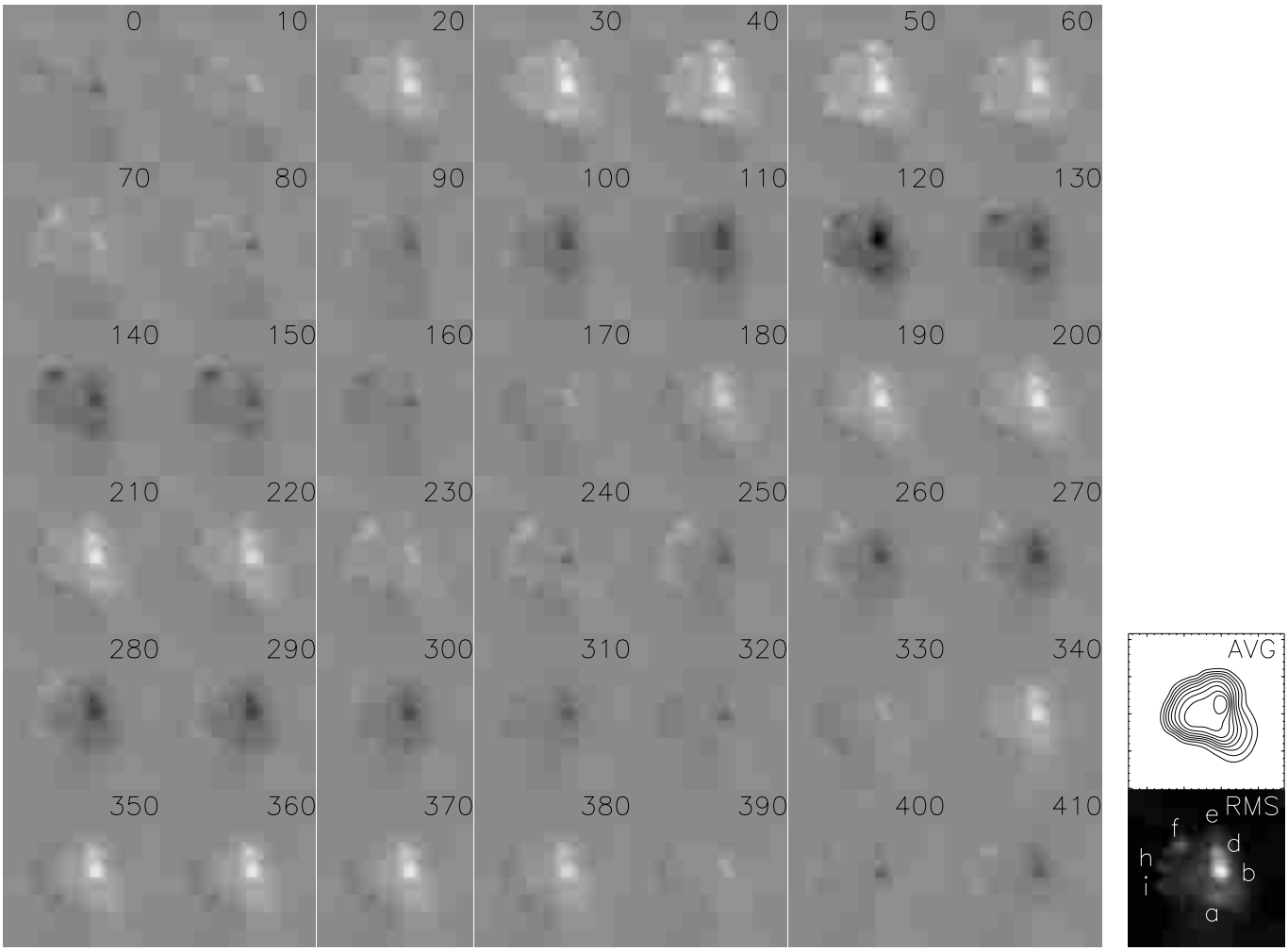

Fig. 3. 8.5 GHz I snapshot difference images (see text for details) obtained every 10 s between 22:19:00–22:26:00 UT. In the rightmost column the average and rms images derived from the entire 22:19:00–22:32:20 UT time series are presented.

localized (the typical size of the fluctuating "patches" is about 2″–4″ at 8.5 GHz and about 3–4.5″ at 5 GHz; thus most of them are unresolved). The patchy appearance of the difference images may reflect inhomogeneities in the sunspot's atmosphere. At 8.5 GHz the strongest I fluctuations (sources b and d in the I rms image) and the strongest V fluctuations (source c in the V rms image) are associated with the region of maximum total intensity. The 8.5 GHz I snapshot images also show a few weaker distinct peaks (labeled a, e, f, h, i in the rms image) located close to the edge of the I average image (most of them at the eastern edge). Except the strong source c, the V images show two weaker sources which are associated with sources a and e of the I images. Of course, the I peaks close to the eastern edge of the average image have no counterparts in the V images because the circular polarization is very weak there due to the presence of the depolarization strip (see Sect. 3). An interesting feature of the 8.5 GHz strongest fluctuating sources is that when their I emission increases the V emission decreases. This effect can be interpreted in terms of the g–r mechanism: e.g. when the magnetic field increases the second harmonic of the gyrofrequency moves higher in hotter regions of the atmosphere and the resulting total intensity emission increases. At the same time, the circular polarization decreases due to the decrease of the difference between the optical depth of the x and the o–mode. Model computations verify this speculation (see Sect. 6).

At 5 GHz all strong fluctuations of I emission are located close to the edge of the I average image which roughly coincides with the penumbral outer border while the strongest fluctuation of the circular polarization is associated with the component in the middle of the average V image. Furthermore, the location of these 5 GHz fluctuating sources is different from the location of the 8.5 GHz patches of strong emission variations. We note that, contrary to what happened at 8.5 GHz, here in all polarized fluctuating elements when the total intensity increases, the corresponding circular polarization also increases.

In the snapshot difference images we made several cuts through the center of the spot and for each cut we displayed the brightness temperature variations as a function of position and time (not shown here for the sake of

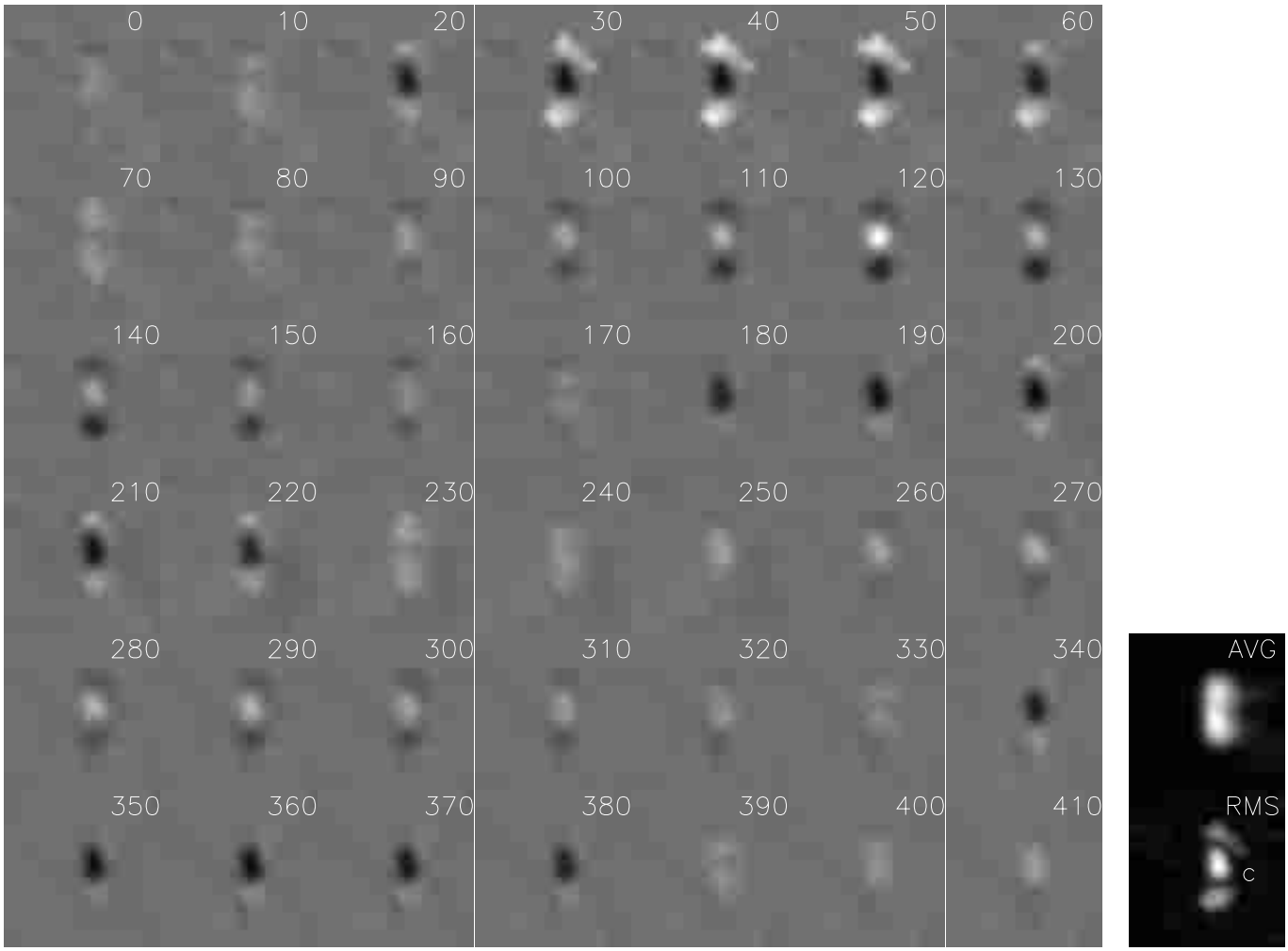

Fig. 4. Same as in Fig. 3 for the 22:19:00–22:26:00 UT 8.5 GHz V snapshot difference images.

brevity). At both frequencies the disturbances associated with most patches of strong fluctuations do not propagate along the cuts. This confirms the impression from the visual inspection of the difference images that the locations of most oscillating patches do not change significantly during the entire time series. Such behavior is completely different from the behavior of chromospheric velocity oscillations which propagate from the umbra to the penumbra (e.g. Alissandrakis et al. 1999; see their Fig. 2).

In Fig. 7 we present the I and V time profiles of the 8.5 GHz fluctuating sources that have been labeled in the rms images of Figs. 3 and 4 together with the total flux time profiles. The resulting power spectra are presented in Fig. 8. The time profiles and power spectra of selected 5 GHz fluctuating sources appear in Figs. 9 and 10. For the computation of all power spectra a 600–s *FWHM* (full width at half maximum) Gaussian taper was applied to the time series. In Tables 2 and 3 we give the oscillation rms amplitude, the maximum power and the frequency where it occurs together with the corresponding phase of the oscillating elements labeled in Figs. 3–6.

The 8.5 and 5 GHz time profiles quantify the results derived from the visual inspection of the difference images of Figs. 3–6. The I time profiles of sources a–d are similar: minima and maxima of the oscillating total intensity occur at about the same time. The V time profiles of sources b, c and d show maxima when the corresponding I time profiles show minima and vice versa. The I time variability of sources e and f is similar and the same is true of the variability of sources i and h. We note that the V minima and maxima of the time profiles of sources a and e occur almost simultaneously with the I minima and maxima. Due to the depolarization effects the V time variations of sources f, h and i are very low. Source b exhibits the strongest I fluctuations: the oscillation rms amplitude is about 1.3×10^5 K. In agreement with Fig. 3, the I oscillation rms amplitude of sources e, f, h and i is lower, around 2–5 $\times 10^4$ K. The strongest V oscillations are associated with source c, their rms amplitude being 2×10^4 K.

Figure 9 shows that the 5 GHz time profiles of the oscillating elements are similar. Only the total intensity minima and maxima of sources I and J are somewhat displaced with respect to the minima and maxima of the other sources. We also note that in all polarized 5 GHz sources the V peaks occur almost simultaneously with the I peaks. Overall the amplitude of the 5 GHz

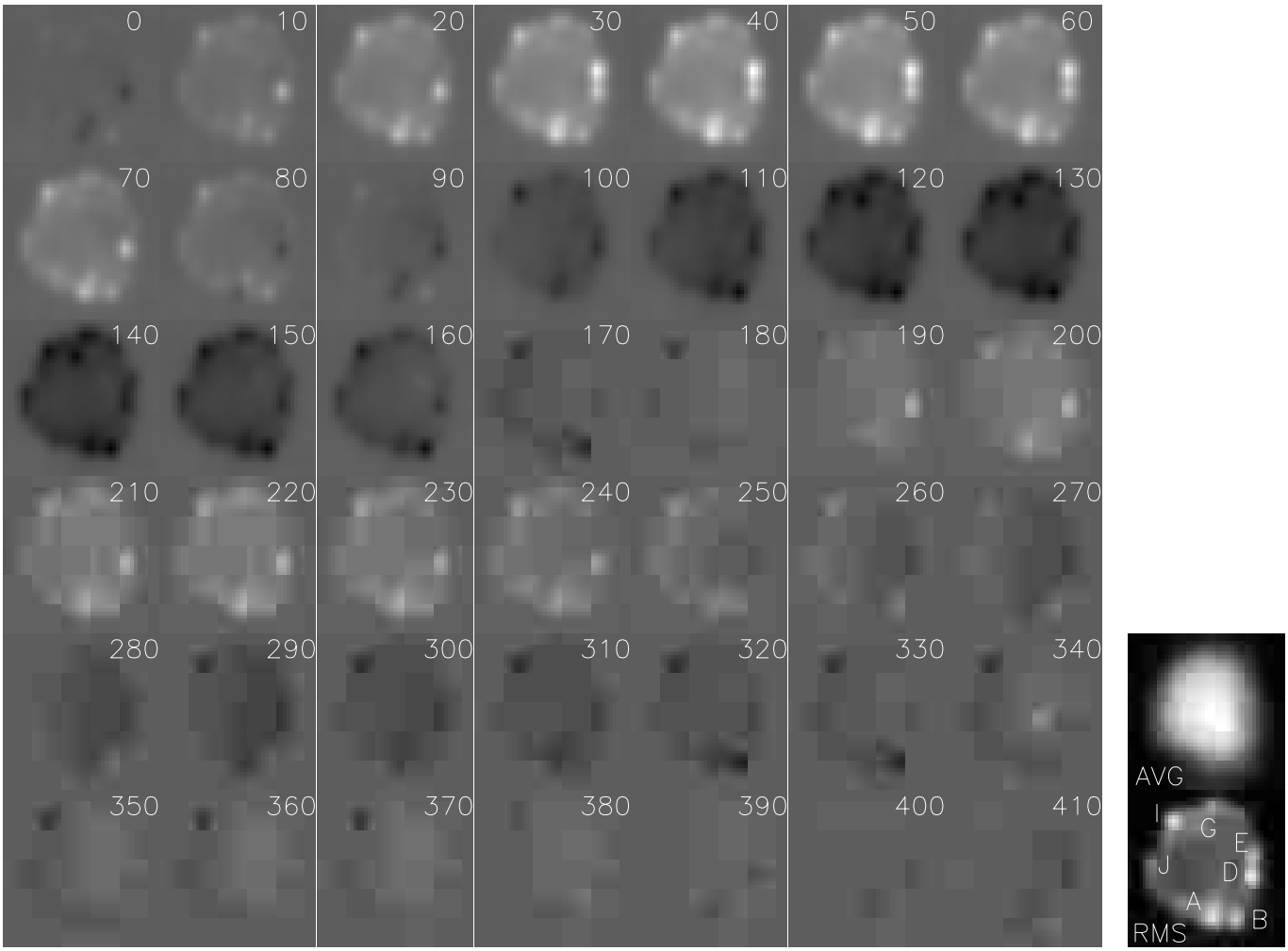

Fig. 5. Same as Fig. 3 for the 5 GHz I snapshot difference images obtained every 10 s between 21:40:00–21:47:00 UT. The average and rms images have been derived from the entire 21:40:00–21:53:20 time series.

oscillations is smaller than the amplitude of the 8.5 GHz oscillations. The rms amplitudes of the I oscillations are between 1.3–2.5 $\times$ 10^4 K while the rms amplitudes of the V oscillations are between 0.3–1.4 $\times$ 10^4 K.

The computed power spectra cover frequencies up to 50 mHz. In order to enhance the visibility of the plots we show the power up to 30 mHz; no significant power was present between 30–50 mHz. Our data show no trace of the 300–s oscillations, in agreement with the result of Shibasaki (2001). We note that in their power spectra Gelfreikh et al. (1999) did detect the presence of 300–s oscillations, but their power was small. In all cases (except the V power spectra of the essentially unpolarized sources) the I and V spectra show a clear power concentration between about 3–8 mHz. Figures 8 and 10 show that the most prominent peaks of oscillatory power occur around 6.25–6.45 mHz (periods of 155–160 s) and around 4.49–5.47 mHz (periods of 183–223 s). The power spectra of 8.5 GHz sources b, c and d show that the strongest oscillatory power is associated with clear peaks around 6.25–6.45 mHz. The two power peaks mentioned above appear with varying relative strengths in most other oscillating patches (except 8.5 GHz sources i and h whose peaks around 5.08–5.47 mHz dominate) and this effect shows better in the 5 GHz power spectra (see also Table 3). It seems that the sunspot's atmosphere is subject to disturbances having slightly different periods: the eastern part is affected mostly by disturbances with periods of 183–213 s while in the western part oscillations with periods of 155–160 s and 183–213 s appear. At 8.5 GHz, sources b, c and d show harmonics of the 3-min oscillations. These harmonics survive in the power spectrum of the V flux but they are very weak in the power spectrum of the I flux. The presence of the relatively weak harmonics implies the presence of weak nonlinear effects. The frequency resolution of our power spectra is 1.25 mHz while the typical $FWHM$ of the power peaks is 1.1–1.7 mHz. The resolved power peaks are associated with the 8.5 GHz oscillations while the 5 GHz power peaks are unresolved.

At each observing frequencies the phases of the 6.25–6.45 mHz I power peaks are similar and the same is true of the phases of the 4.49–5.27 mHz I power peaks. We note that all phases that appear in Tables 2–3 have been computed with respect to 22:19:00 UT. The computed phases

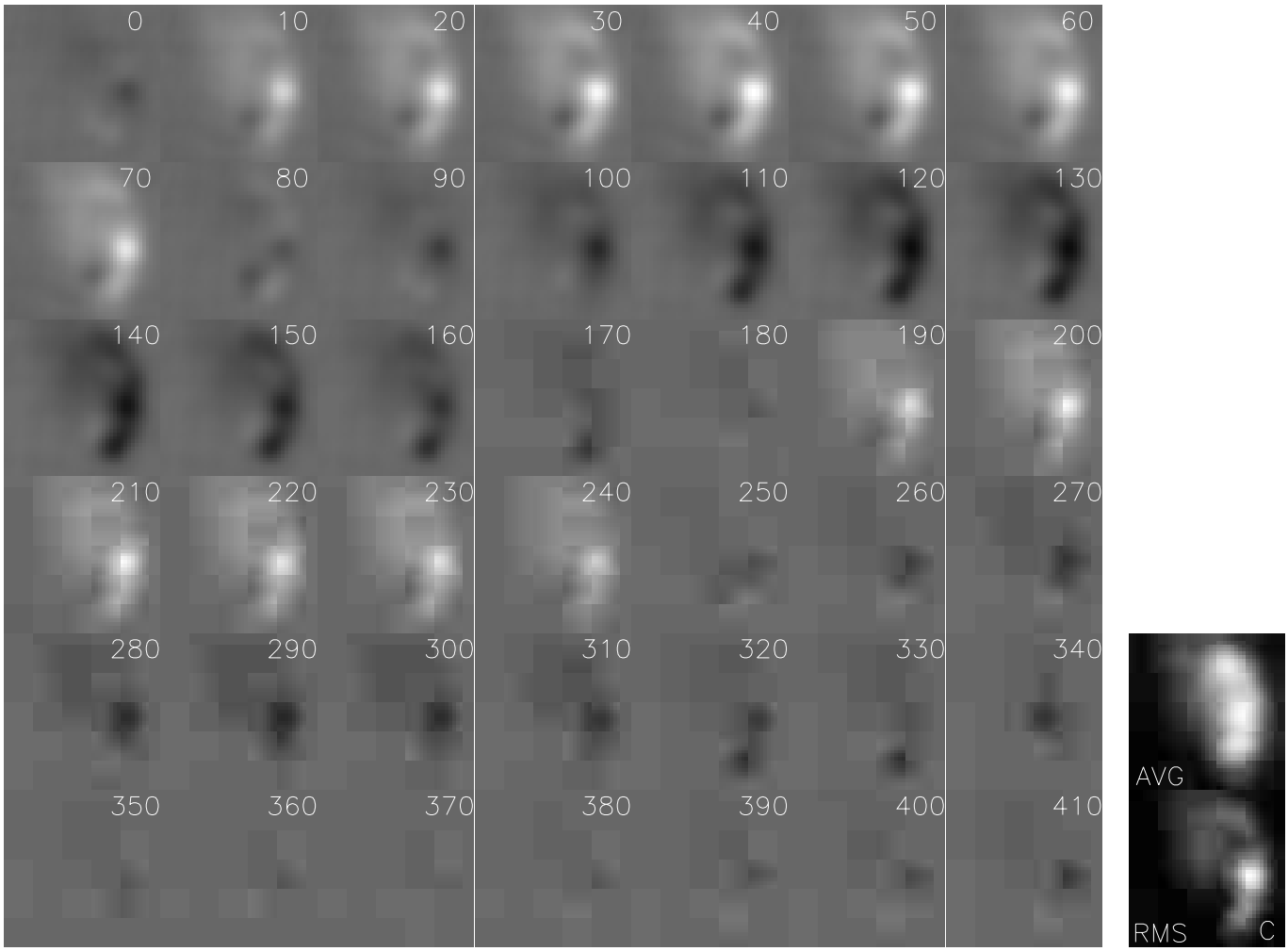

Fig. 6. Same as in Fig. 5 for the 21:40:00–21:47:00 UT 5 GHz V snapshot difference images.

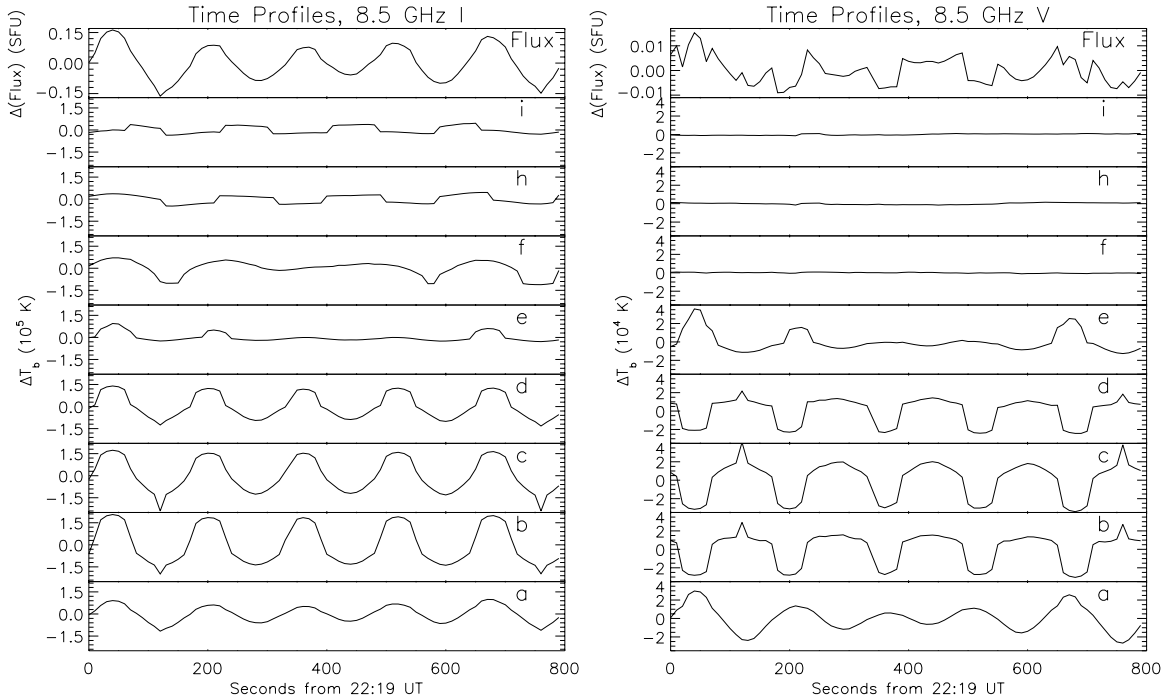

Fig. 7. Time profiles of the 8.5 GHz I and V fluctuating sources that have been labeled in the rms image of Figs. 3 and 4.

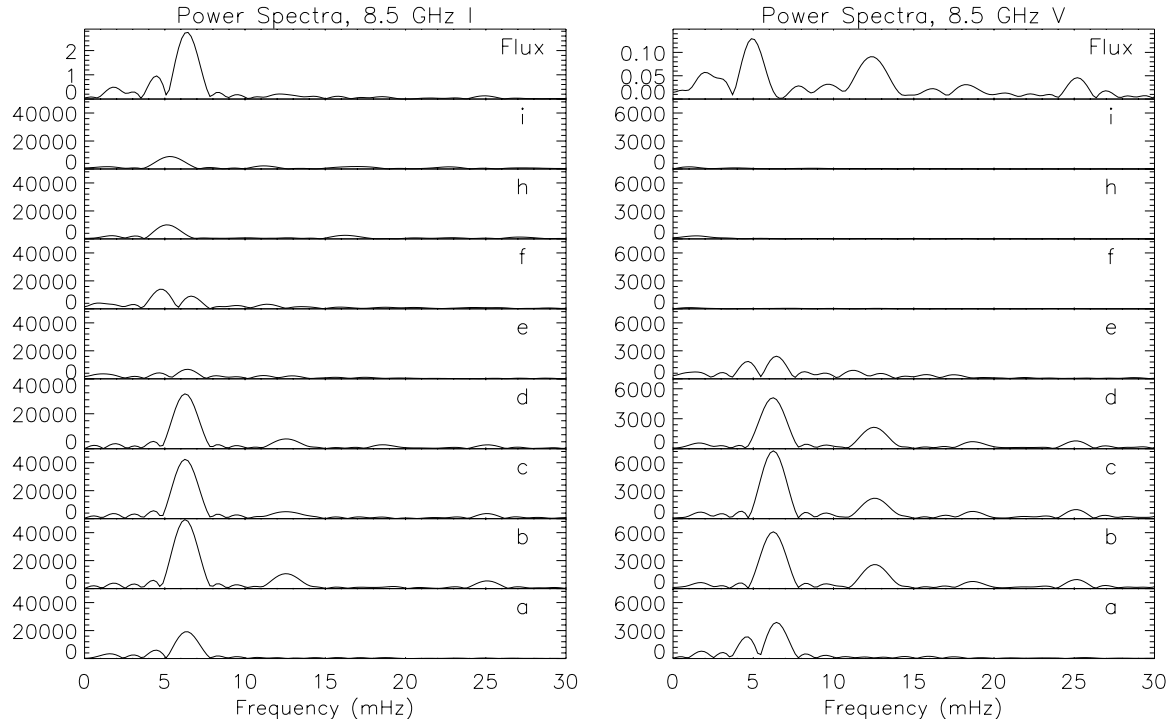

Fig. 8. Power spectra resulting from the time profiles presented in Fig. 7. The power is expressed in units of $10^2\times$ K/Hz for the individual sources and in SFU/Hz for the flux.

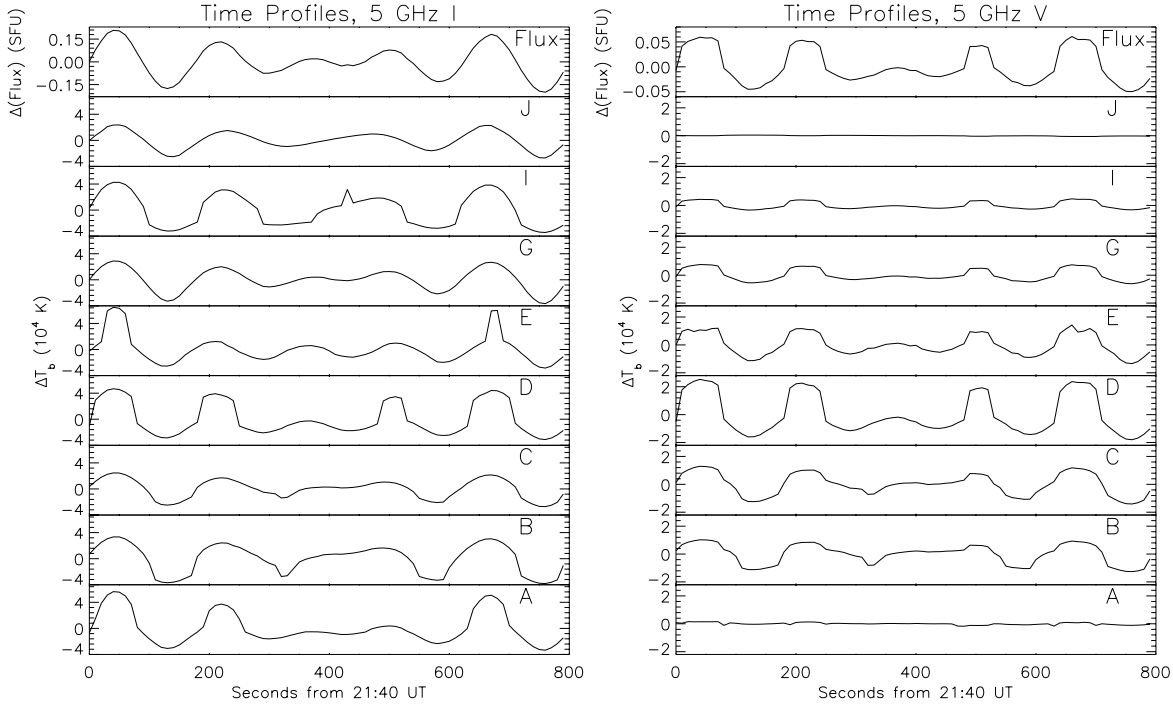

Fig. 9. Time profiles of the 5 GHz I and V fluctuating sources that have been labeled in the rms image of Figs. 5 and 6.

show that there is a $\sim$180° phase difference between the total intensity and circular polarization oscillations of the 8.5 GHz sources associated with the peak of the 8.5 GHz I average image (sources b, c and d). Since these are the strongest oscillations at 8.5 GHz, there is no surprise that a similar phase difference exists between the phase of the 8.5 GHz I flux power maximum and the phase of the 8.5 GHz V flux power maximum.

Let us go back now to the shorter duration oscillations. In Table 1 we gave the I flux rms amplitude together with phase estimations for the shorter duration radio fluctuations detected during the observations. Since most of these time intervals were short, a power spectrum analysis cannot give reliable results. Thus a rough estimation of the associated phases was done by fitting sinusoidal curves with periods of 155–160 s to the I flux time

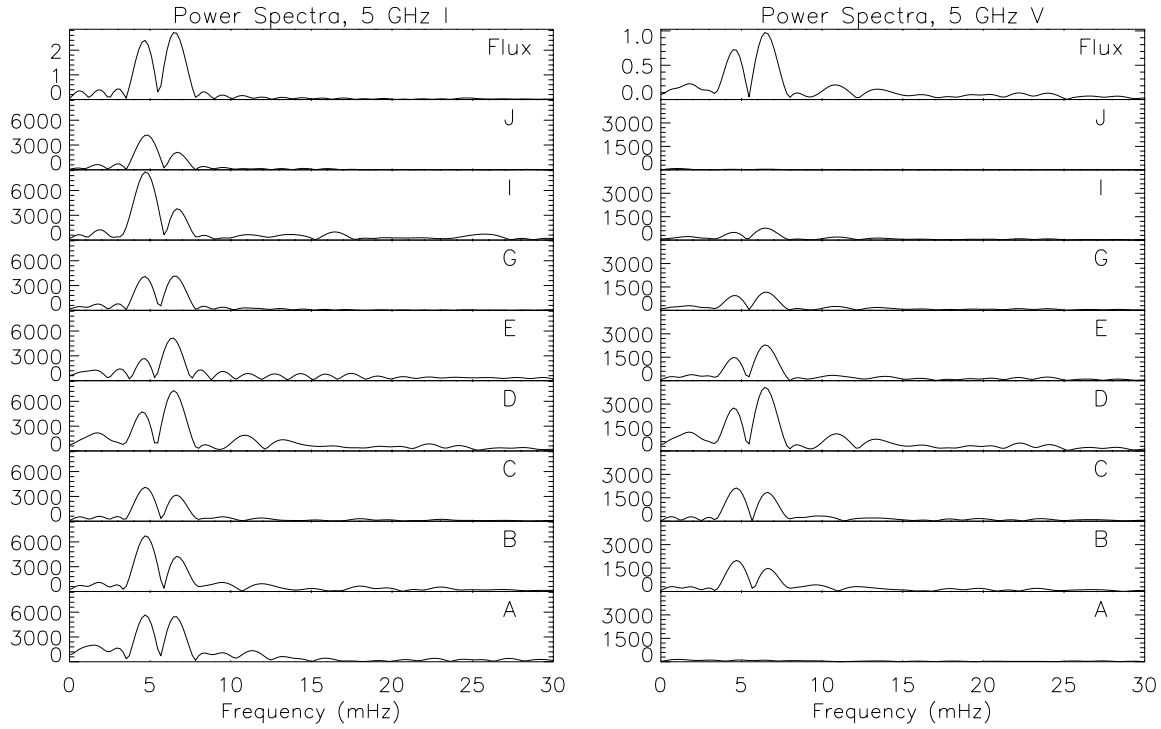

Fig. 10. Power spectra resulting from the time profiles presented in Fig. 9. The units are the same as in Fig. 8.

profiles. For the sake of completeness, the same procedure was also applied to the 800–s–long flux time profiles discussed above. All phases were computed with respect to 22:19:00 UT. Table 1 indicates that when the fluctuations occur, in addition to their positional stability (see Fig. 2), they show significant amplitude and phase stability (at least the 8.5 GHz phases; at 5 GHz the scatter in the computed phases is larger and is probably associated with the presence of the strong 4.49–4.68 mHz power component).

The total duration of oscillatory fluctuations, however, is only a fraction of the total solar observing time (about 19% at 8.5 GHz and 21% at 5 GHz if we do not consider the time intervals that we flagged), contrary to the results of Shibasaki (2001) who detected 17 GHz oscillations above a sunspot for more than 7 hours. We have only two time series, one at 8.5 and one at 5 GHz, where oscillations were observed throughout a solar scan (the time series studied above). Unfortunately in addition to calibration scans, the above scans were sandwiched by 15 GHz solar scans. In other scans (the time profile presented in Fig. 2 is a typical example) the oscillations start rather suddenly and the intensity returns to levels roughly equal to the intensity before the oscillation somehow more gradually. During the time that the oscillation dies out a few low intensity peaks ($\sim$1.5–2$\times10^4$ K at 8.5 GHz) do occur but we are not able to establish a clear periodic trend for the time of their appearance. The absence of fluctuations with amplitudes similar to the ones presented in Figs. 7 and 9 cannot be attributed to excess noise levels because during each scan the noise level of the snapshot images did not change significantly. Therefore it seems that these oscillations die out from time to time and are re–excited later. In that respect our observations resemble Rüedi & Solanki's (1999) results who detected intermittent oscillations of the photospheric magnetic field of a sunspot. Of course we cannot rule out the possibility of the occurrence of oscillations even when we do not detect them provided that their amplitude is smaller than the typical rms amplitude of emission variations (about 4000–9000 K).

5. Reliability of results

In this section we discuss whether the oscillations seen in the 8.5 and 5 GHz I and V images come from non–physical sources (i.e. data analysis errors and/or instrumental origin). We are confident that the observed oscillations of the radio emission reflect physical variations in the atmosphere above the sunspot for four reasons:

(1) At both frequencies we computed the I and V time profiles of selected background pixels in several areas of the snapshot maps away from the sunspot–associated source. Both the visual inspection of the resulting time profiles and the power spectrum analysis showed no trace of oscillations. Furthermore the rms values of the background intensity fluctuations was very small (about 0.20% at 5 GHz and 0.62% at 8.5 GHz).

(2) We computed time profiles of the emission from active region NOAA 8948 which was close to the west edge of the 5 GHz field of view. According to the MDI images, this active region underwent rapid changes associated with the emergence of new magnetic flux. The time profiles of the 5 GHz emission reflected those changes: for most radio components the total intensity increased continuously

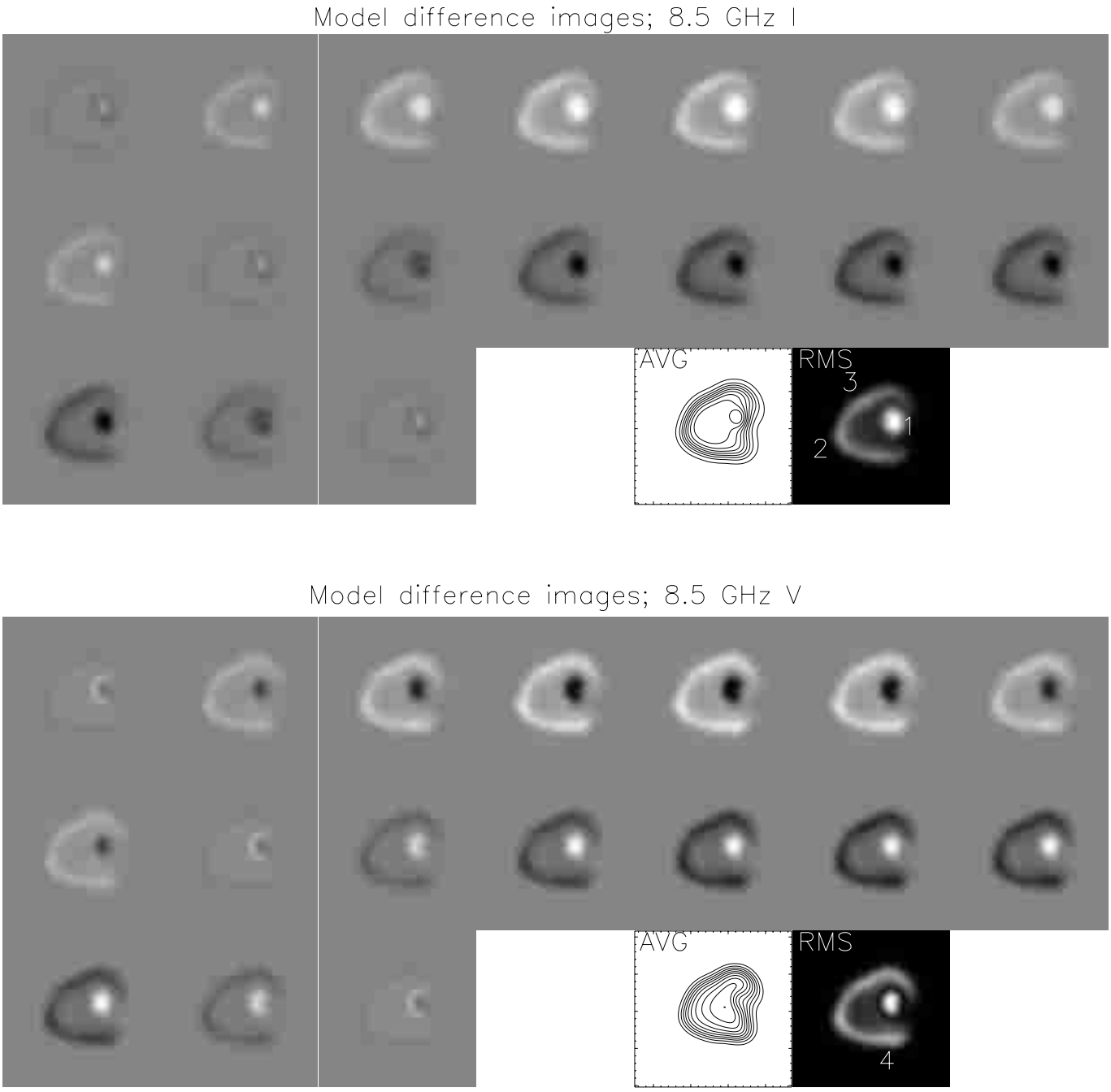

Fig. 11. A full period of 8.5 GHz I and V model difference images derived after the application of a sinusoidal variation of the photospheric magnetic field strength with period of 160 s and rms amplitude of 40 G. In the third and bottom rows we also show the I and V average best–fit models (see text for details) and the resulting rms images.

while the circular polarization decreased. The resulting power spectra confirmed that no oscillations were present.

(3) We tried a different technique for the production of the snapshot difference images. At each frequency we produced images using the whole time interval where oscillations were present. Then the clean components of these maps were subtracted from the self–calibrated visibilities. This technique generally does not remove large–scale flux very well since it is not as well represented by the clean components. However, Figs. 3–6 show that the maximum oscillating power comes from relatively compact sources, so we mapped the resulting visibilities using only the longer baselines (see Nindos et al. 1999). This method reproduces successfully the patchy oscillating elements that appear in Figs. 2–6: the resulting time profiles show differences of about 10–15% compared to the time profiles presented in Figs. 7 and 9. Furthermore the power spectrum analysis yields the same peaks that we derived in Sect. 4.

(4) We also produced snapshot maps without using self–calibration. From each visibility timestamp, we subtracted the time–average visiblity of the whole scan.

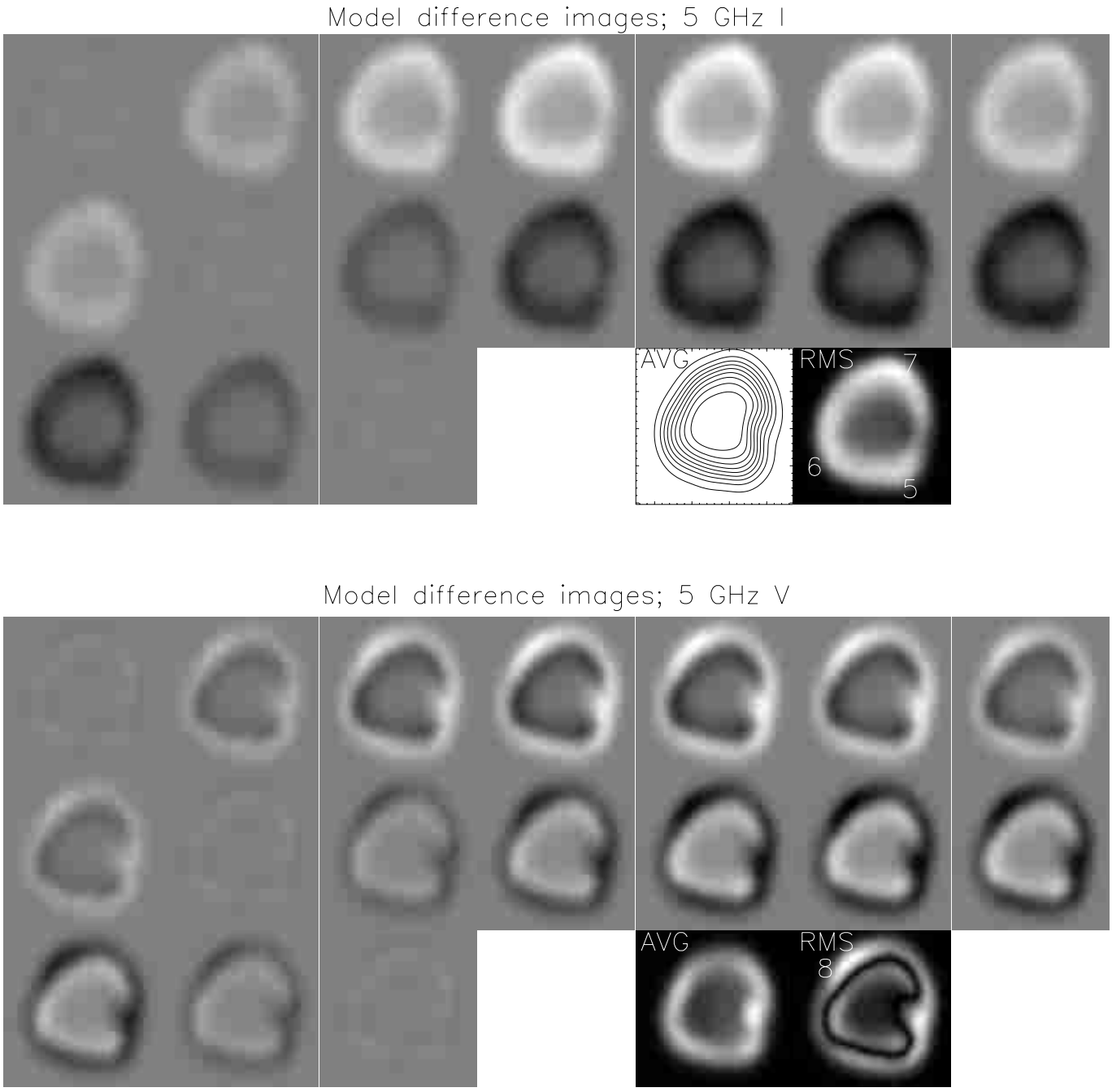

Fig. 12. Same as in Fig. 11 for the 5 GHz I and V model difference images.

The resulting visibilities were mapped and then the dirty maps were cleaned as usually. We attempted no self–calibration in order to check whether self–calibration influenced our results. As expected the dynamic range of the resulting snapshot maps was lower than the dynamic range of the maps that we presented in Sect. 4. However, in all of them the bright oscillating elements are reproduced and their time variability is consistent with the time variability of the corresponding sources in Figs. 3–6.

6. Model computations

At 8.5 and 5 GHz, gyroresonance is the dominant emission mechanism of sunspot–associated sources with brightness temperatures of the order of 10^6 K; the contribution of the free–free mechanism is much smaller. Gyroresonance is a resonant mechanism: opacity is significant only in thin layers where the observing frequency is a low–integer multiple of the local gyrofrequency. The g–r emission in the x mode comes primarily from the third or lower harmonics of the gyrofrequency, whereas o mode emission has less opacity and comes from the second harmonic. The structure of the source depends upon which of the low–order (second to fourth) harmonics of the gyrofrequency are located in regions of high temperature. This, in turn, depends on the frequency and the magnetic field. The brightness temperature of a harmonic that satisfies the above condition

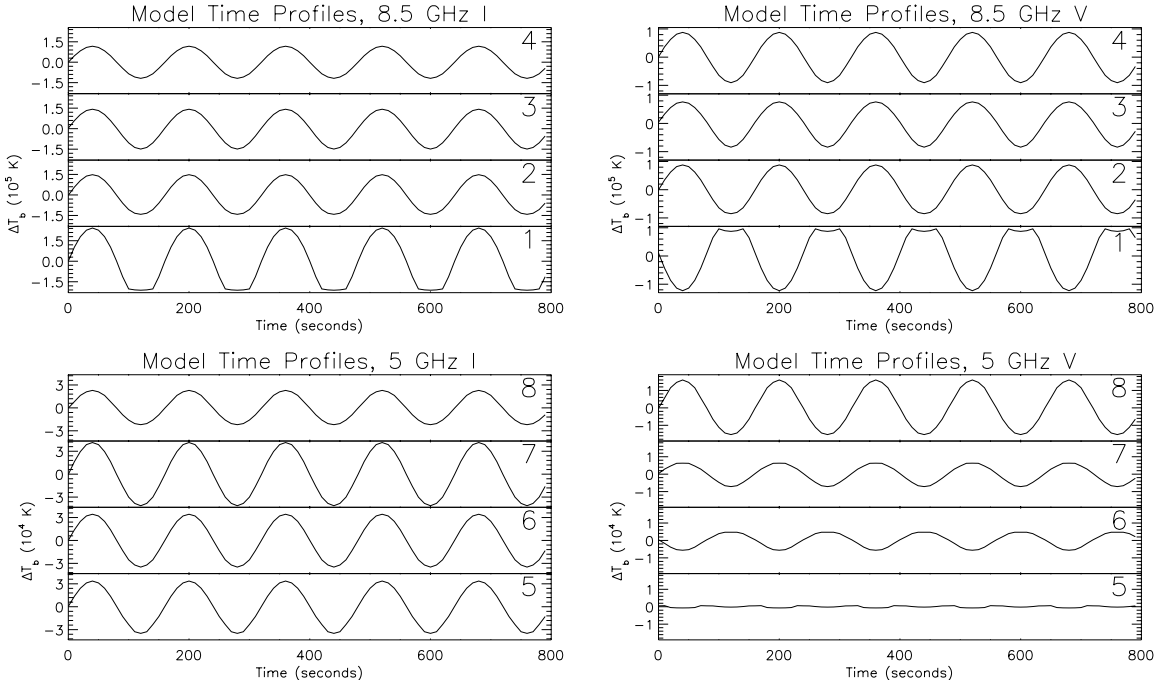

Fig. 13. Time profiles of the model fluctuating sources that have been labeled in the rms images of Figs. 11 and 12.

is determined by the electron temperature at the height where it is located and by its opacity. The opacity has much stronger dependence on the angle θ between the magnetic field and the line of sight than on any other physical parameter such as temperature and density.

We made model computations of the microwave emission in order to determine the factors that contribute to the observed variations of the sunspot's microwave emission. The microwave emission in the x and o modes is computed by intergration of the transfer equation, taking into account thermal free–free and g–r emission and absorption up to the fourth harmonic (for details see Alissandrakis et al. 1980). The computation requires knowledge of the electron temparature, pressure and magnetic field in the TR and the low corona. The temperature structure in the region from 10^5 K up to the corona (which is assumed isothermal with electron temperature $T_{\rm cor} = 3.3{\times}10^6$ K) is determined by the assumption of constant conductive flux $F_{\rm c}$. The computation of pressure as a function of height is done under the assumption of hydrostatic equilibrium. The magnetic field is obtained from constant–α force–free extrapolations of the photospheric magnetic field from MDI. We compute the field up to a height of 3.2×10^4 km above the photosphere using the method developed by Alissandrakis (1981).

The model is therefore determined by the following free parameters: the conductive flux $F_{\rm c}$, the height h_0 of the $T = 10^5$ K level (we shall call it the "base of the transition region"), the pressure p_0 at height h_0 and the value of α. The best–fit model should reproduce the spatial structure and total flux of both average I maps presented in Figs. 3 and 5. Our model does not take into account propagation effects therefore the observed characteristics of the V maps cannot be reproduced. The best–fit values are $F_{\rm c} = 6 \times 10^6$ erg cm^{-2} s^{-1}, $h_0 =$ 2000 km, $p_0 = 2 \times 10^{15}$ cm^{-3} K and $\alpha = 0$. We note that in this model we have multiplied the umbral magnetic field by a factor of 1.9 at all levels: without this correction the 8.5 GHz models show no g–r emission (see also Alissandrakis et al. 1980; Nindos et al. 1996). The resulting model maps are labeled "AVG" in Figs. 11 and 12. These I models reproduce satisfactorily the observed characteristics of the average maps at both frequencies but, as expected, the V models do not agree with the observations. At 8.5 GHz a small part of the second harmonic surface has entered the TR and it shows up as the peak of the I model map. At 5 GHz the I maximum is broader because the third and second harmonic surfaces have moved higher in hotter regions of the atmosphere.

Subsequently, we made sequences of model maps applying sinusoidal variations, same for all pixels, of the photospheric magnetic field strength around the observed magnetogram values with period of 160 s and time resolution 10 s. We also made separate sequences of model maps applying similar sinusoidal variations of the conductive flux, the pressure p_0 and the height of the base of the TR h_0 around their best–fit model values. From all resulting model maps the appropriate "average" best–fit model map was subtracted. The resulting model difference images and the model oscillation amplitudes were compared with the observations. The best agreement is reached when we vary the magnetic field strength and/or the height of the base of the TR. In Figs. 11 and 12 we show a full period of model difference images derived after the application of a sinusoidal variation of the photospheric magnetic field strength with rms amplitude of 40 G. This is our best–fit model difference image sequence: it reproduces well several spatial features of the observed radio oscillations and

the oscillation amplitudes (see Fig. 13) are broadly consistent with the amplitudes of the observed oscillations. We note however that the appearance of the model difference images is not patchy contrary to the observations. This is not a surprise because all models have been convolved with the appropriate VLA beam which is larger than most observed patches.

The 8.5 GHz model difference images (Fig. 11) show that the strongest microwave fluctuations occur at the region of the I peak. When the model intensity of this region increases the circular polarization decreases in agreement with the observations. Our modeling verifies the interpretation we presented in Sect. 4: when the magnetic field increases the second harmonic moves in hotter regions and the resulting total intensity emission increases. But the circular polarization decreases because the difference between the optical depth of the x and the o mode decreases. The I and V time profiles of source "1" (Fig. 13) show that the phase difference between the total intensity and circular polarization oscillations is almost 180° in remarkable agreement with the observations. The intensity of the outer border of the 8.5 GHz model source also fluctuates but with smaller amplitudes (see the time profiles of sources 2, 3 and 4 in Fig. 13). Here the magnetic field is such that only the third harmonic has entered the TR. Consequently, when the magnetic field increases the resulting x-mode emission increases while the o–mode emission is very small. Therefore both the I and V emissions increase.

At 5 GHz the models show that different regions oscillate. In agreement with the observations, oscillations of the radio emission appear at the border of the 5 GHz source (Fig. 12). The model time profiles reproduce the observational result that overall the amplitude of the 5 GHz oscillations is smaller than the amplitude of the 8.5 GHz oscillations. The outer part of the 5 GHz oscillation "ring" is associated with regions where only the third harmonic is above the TR and consequently when the I emission increases the V emission also increases (see the 5 GHz time profiles of Fig. 13). However, in most of the inner part of the oscillation "ring" when the total intensity increases the circular polarization decreases due to the appearance of the second harmonic in the TR. This is not consistent with the observations. However we note that the eastern part of the 5 GHz VLA maps is essentially unpolarized and we do not know how they would appear if they were not influenced by propagation effects.

Model difference images with similar structures can be derived using rms amplitudes for the magnetic field strength oscillation between 4–130 G. But an rms amplitude of 40 G which is equivalent to a 2.5% relative variation, yields model radio oscillation amplitudes that fit best the amplitudes of the observed oscillations. We also note that exactly the same oscillations of the radio emission can be obtained if we vary the height of the base of the TR appropriately, instead of the magnetic field strength. For example exactly the same results presented in Figs. 11–13 can be obtained if the rms amplitude of the h_0 oscillation is 25 km. From the point of view of the model code, both effects are equivalent because changes in the source's structure occur when the location of the third and/or second harmonic surfaces changes with respect to the base of the TR.

Varying the pressure p_0 at the base of the TR or the conductive flux F_c yields microwave oscillations whose features do not match the observations. Pressure variations affect most the intensity of the borders of the source: this is consistent with the 5 GHz observed oscillations but disagrees with the 8.5 GHz oscillations because the region of maximum intensity is not affected. Furthermore, the resulting oscillations at both frequencies show similar amplitudes contrary to the observarions. In order to reproduce the maximum amplitudes of the observed total flux oscillations we need pressure variations with rms amplitudes of 4.3–5 $\times 10^{14}$ cm^{-3} K which is highly unlikely (e.g. see the results by Brynildsen et al. 1999a). Therefore our modeling confirms that at such high frequencies pressure does not play a significant role in the determination of the structure of sunspot–associated sources (e.g. see Nindos et al. 1996). The conductive flux variations yield I oscillations that affect the entire source because the temperature structure in the TR is determined by the assumption of constant F_c. The maximum amplitudes of the observed I total flux oscillations are reproduced by F_c variations with rms amplitudes of 1.2×10^6 erg cm^{-2} s^{-1} at 8.5 GHz and 0.6×10^6 erg cm^{-2} s^{-1} at 5 GHz. Such large variations of the pressure and conductive flux should have generated significant nonlinear effects and the resulting power spectra should have shown much stronger harmonics of the 3–min oscillations.

Finally we computed model maps of the 15 GHz emission using the best–fit average model parameters described above. The models confirm that the 15 GHz emission comes from the free–free mechanism. The VLA data did not show oscillations at this frequency but if they existed their amplitude should have been below 1100–1500 K (see Sect. 3). In our models this level is not exceeded if the relative amplitude of pressure variations is less than 1%.

7. Discussion

Using high quality VLA observations, we detected spatially resolved oscillations in the 8.5 and 5 GHz I and V emission of a sunspot–associated g–r source. The same phenomenon has been detected in 17 GHz flux time profiles from NoRH observations (Gelfreikh et al. 1999; Shibasaki 2001). Usually the fine structure of g–r sources is below the spatial resolution of the NoRH snapshot maps and thus only variations of the total I and V flux can be studied reliably with the NoRH.

The detected oscillations are intermittent. Despite their transient nature, when observed they revealed significant positional as well as amplitude and phase stability. The oscillations start rather suddenly and they die out somehow more gradually. Given that the noise level does

not change significantly during each solar scan, this means either that the oscillations disappear completely from time to time and are re–excited later or that they are always present (with smaller amplitudes than the typical rms amplitude of emission variations) and from time to time they are amplified. The largest part of this paper was dedicated to the analysis of the longest uninterrupted oscillation time series; the shorter duration oscillations showed similar properties.

At both frequencies the spatial distribution of intensity variations is far from homogeneous. The snapshot difference images do show that the intensity above the whole sunspot changes as a function of time but clearly some areas of the source are associated with stronger fluctuations. During all time intervals where oscillations were detected, at each frequency the strong fluctuations reoccur at the same locations. The patchy appearance of oscillatory power may reflect inhomogeneities in the sunspot's atmosphere. The strongest oscillations are associated with the peak of the 8.5 GHz I average map while distinct peaks of weaker oscillatory power appear close to the outer boundaries of the 8.5 and 5 GHz g–r sources. Therefore the spatial distribution of the microwave oscillation power does not resemble the well known chromospheric velocity oscillations; it is closer to the spatial distribution of oscillations of the photospheric magnetic field strength (however, these magnetic field oscillations are more localized than ours: e.g. see Rüedi et al. 1998; Balthasar 1999). Overall the 5 GHz oscillations are weaker than the 8.5 GHz oscillations (the rms amplitudes of the I oscillations are 1.3–2.5 $\times$ 10^4 K and 0.2–1.5 $\times$ 10^5 K respectively).

The strongest oscillation power is associated with variations of the location of the 8.5 GHz second harmonic surface with respect to the base of the TR: therefore when the I emission increases the V emission decreases and our models reproduce the observed 180° phase difference between the I and V oscillations. The other oscillation peaks are associated with similar variations of the third harmonic location.

In terms of photospheric magnetic field variations, the best fit model to the oscillations can be derived from magnetic field strength oscillations with an rms amplitude of 40 G, much larger than the rms amplitudes of 6–7 G derived by Rüedi et al. (1998) and Norton et al. (1999) but in rough agreement with the results of Balthasar (1999) who reported variations with rms amplitudes of 40–50 G. We note that our sunspot is much smaller than the sunspots studied by Rüedi et al. (1998) and Norton et al. (1999) and that model calculations by Zhugzhda et al. (2000) suggest that small sunspots produce large magnetic field strength oscillation amplitudes and vice versa. Instead of using magnetic field variations, the above best–fit model can be derived from oscillations of the height of the base of the TR with rms amplitude of 25 km.

If we assume that the microwave oscillations are caused by magnetic field oscillations, the question that arises is whether they are due to oscillations of the magnetic field strength (magnetoacoustic gravity waves) or due to oscillations of the orientation of the magnetic field vector (Alfven waves). Changing the heliographic distance of the sunspot's photospheric magnetic field used in the force–free extrapololations provides a crude way to check the Alfven wave hypothesis. Unfortunately the modeling is not conclusive: a 1° variation of the heliographic distance yields variations in the model maps that are consistent with the model map variations presented in Figs. 11 and 12 and the time profiles presented in Fig. 13. The morphology of the microwave variations gives an upper limit of 4–4.5° in the variation of the heliographic distance that produces similar structures. But a ∼1° variation yields model radio oscillations that are consistent with both the structure and the amplitudes of the observed oscillations. Therefore, our data suggest that if the microwave oscillations come from directional oscillations of the magnetic field vector, the amplitude of such magnetic field direction oscillations should be very small. Consequently our dataset cannot determine unequivocally whethere the observed oscillations are due to magnetoacoustic gravity waves or due to Alfven waves. For this problem additional information from velocity oscillations would be valuable because in the Alfven waves the magnetic and velocity signals are expected to oscillate in phase while in the magnetoacoustic gravity waves the phase difference should be 90°.

We have detected radio intensity oscillations at different heights above the sunspot; therefore the question of the propagation of the disturbance with height arises. Using the calculated phases of the maximum I flux power peaks at 8.5 and 5 GHz we find a phase difference of 139° between the two oscillations. Furthermore the models provide the heights of the gyroresonant surfaces. However there is no overlap between the regions where the 5 GHz total flux oscillations come from and the regions where the 8.5 GHz flux oscillations come from and therefore no reliable computation of the phase velocity of the disturbance can be made; all we can say is that the 8.5 GHz oscillations lead the 5 GHz oscillations. This problem can be addressed if simultaneous observations of oscillations at two frequencies are available. Such dataset can be obtained if the VLA is split into two "subarrays" observing at different frequencies at the cost of reduced mapping ability. Such observations will not be able to reveal the fine structure of the oscillatory power presented here but nevertheless the simultaneous total flux oscillations, if present, should be useful.

8. Conclusions

The excellent VLA spatial resolution allowed us, for the first time, to study the spatial distribution of microwave oscillatory power above a sunspot. Our results can be summarized as follows:

(1) Total intensity and circular polarization oscillations were detected at 8.5 and 5 GHz during several time intervals of the observing run. The oscillations are intermittent.

(2) Despite their transient nature, when they occur they show significant positional as well as amplitude and phase stability.

(3) At both frequencies the spatial distribution of intensity variations is patchy. During all time intervals where oscillations were detected, at each frequency the strong fluctuations reoccur at the same locations. Furthermore, the location of these patches is not the same at both frequencies.

(4) The 5 GHz oscillations are weaker than the 8.5 GHz oscillations.

(5) The power spectra show peaks at 6.25–6.45 mHz and 4.49–5.47 mHz. The phases of the oscillation power peaks show significant coherence. At each frequency the phases of the 6.25–6.45 mHz I power peaks are similar and the same is true of the phases of the 4.49–5.47 mHz I power peaks. There is, however, a $\sim 180^\circ$ phase difference between the I and V oscillations of the 8.5 GHz sources associated with the average image I peak.

(6) The oscillations are caused by variations of the location of the third and/or second harmonic surfaces with respect to the base of the TR, i.e. either the magnetic field strength or/and the height of the base of the TR oscillates. Our best–fit model shows that the observed radio oscillations can be reproduced by magnetic field strength oscillations with rms amplitude of 40 G or oscillations of the height of the base of TR with rms amplitude of 25 km. The observed oscillations are also consistent with small variations of the orientation of the magnetic field vector.

The detection of microwave oscillations above sunspots with the VLA provides a sensitive tool for high spatial resolution coronal diagnostics because small changes in physical parameters can produce them. In future studies additional simultaneous photospheric and chromospheric high spatial and time resolution observations together with EUV line observations would be desirable.

Acknowledgements. AN would like to thank Dr. S. M. White for his help during the selection of the observed active region. This research at the University of Ioannina and Pulkovo Observatory was carried out with support from European Union's grant INTAS 00-543.

References

Alissandrakis, C. E. 1981, A&A, 100, 197
Alissandrakis, C. E., Kundu, M. R., & Lantos, P. 1980, A&A, 82, 30
Alissandrakis, C. E., Borgioli, F., Chiuder–Drago, F., Hagyard, M., & Shibasaki, K. 1996, Sol. Phys., 167, 167
Alissandrakis, C. E., Tsiropoula, G., & Mein, P. 1999, in ESA SP–448, Proceedings of 9th European Meeting on Solar Physics Magnetic Fields and Solar Processes (Florence, Italy), 217
Balthasar, H. 1999, Sol. Phys., 187, 389
Bellot Rubio, L. R., Collados, M., Ruiz Cobo, B., & Rodriguez Hidalgo, I. 2000, ApJ, 534, 989
Brynildsen, N., Leifsen, T., Kjeldseth–Moe, O., Maltby, P., & Wilhelm, K. 1999a, ApJ, 511, L121
Brynildsen, N., Kjeldseth–Moe, O., Maltby, P., & Wilhelm, K. 1999b, ApJ, 517, L159
Fludra, A. 1999, A&A, 344, L75
Gelfreikh, G. B., Grechnev, V. V., Kosugi, T., & Shibasaki, K. 1999, Sol. Phys., 185, 177
Kundu, M. R., Nindos, A., White, S. M., & Grechnev, V. V. 2001, ApJ, 557, 880
Lites, B. W. 1992, in Sunspots: Theory and Observations, ed. J. H. Thomas, & N. O. Weiss (Kluwer, Dordrecht), 261
Maltby, P., Brynildsen, N., Fredvik, T., Kjeldseth–Moe, O., & Wilhelm, K. 1999, Sol. Phys., 190, 437
Nakajima, H., Nishio, M., Enome, S., et al. 1994, Proc IEEE, 82, 705
Napier, P. J., Thompson, A. R., & Ekers, R. D. 1983, Proc. IEEE, 71, 1295
Nindos, A., Alissandrakis, C. E., Gelfreikh, G. B., et al. 1996, Sol. Phys., 166, 57
Nindos, A., Kundu, M. R., & White, S. M., 1999, ApJ, 513, 983
Nindos, A., Kundu, M. R., White, S. M., et al. 1999, ApJ, 527, 415
Nindos, A., Kundu, M. R., White, S. M., Shibasaki, K., & Gopalswamy, N. 2000, ApJS, 130, 485
Norton, A., Ulrich, R. K., Bush, R. I., & Tarbell, T. D. 1999, A&A, 518, L123
Rüedi, I., Solanki, S. K., Stenflo, J. O., Tarbell, T., & Scherrer, P. H. 1998, A&A, 335, L97
Rüedi, I., & Solanki, S. K. 1999, in 3rd Advances in Solar Physics Euroconference: Magnetic Fields and Oscillations, ed. B. Schmieder, A. Hofmann, & J. Staude, ASP Conf. Ser., 184, 131
Shibasaki, K. 2001, ApJ, 550, 326
Staude, J. 1999, in 3rd Advances in Solar Physics Euroconference: Magnetic Fields and Oscillations, ed. B. Schmieder, A. Hofmann, & J. Staude, ASP Conf. Ser., 184, 113
Tsiropoula, G., Alissandrakis, C. E., & Mein, P. 2000, A&A, 355, 375
White, S. M., & Kundu, M. R. 1997, Sol. Phys., 174, 31
Zhugzhda, Y., Balthasar, H., & Staude, J. 2000, A&A, 355, 347